Solid State Deuteron NMR Studies of Polyamidoamine Dendrimer Salts. 1. Structure and Hydrogen Bonding

Dariya I. Malyarenko,† Robert L. Vold,*,† and Gina L. Hoatson‡

Departments of Applied Science and Physics, The College of William and Mary, P.O. Box 8795, Williamsburg, Virginia 23187-8795

Received September 23, 1999; Revised Manuscript Received December 13, 1999

ABSTRACT: Temperature dependent deuteron quadrupole echo line shapes are reported for integer generations, $G = 1, 2, 3, 5, 7, 9$, of polyamidoammonium chloride salts. The spectra are characteristic of amorphous materials undergoing broad glass transitions between 25 and 65 °C. Adequate fits of room-temperature line shapes were obtained by assuming Gaussian distributions of hydrogen bond lengths for interior $R_2ND\cdots O$ and $R_3ND^+\cdots Cl^-$ deuterons in the dendrimer spacers and Gaussian distributions of librational cone angles for motion of the C_{3v} axes of terminal RND_3^+ groups. The estimated average hydrogen bond lengths at both types of interior site are 2.2 ± 0.15 Å, independent of generation number. For $G = 2$ the spectra obtained upon anion substitution of Cl^- by Br^- demonstrate that both types of hydrogen bonding are counterion dependent. In the temperature range from −30 to 60 °C the decreases in quadrupole coupling constants and increases in observed asymmetry parameters at the interior sites are ascribed to effects of planar libration. In the dendrimer interior the average amplitude of planar libration increases with temperature and decreases with increasing generation. Thermal energy is dissipated in counterion mobility for low generations and in mobility of the dendrimer spacers for high generations. In addition to 3-fold rotation, asymmetric cone libration is required to explain the observed temperature dependent asymmetry parameters of terminal ND_3^+ groups. For both low- and high-generation dendrimers the terminal groups buried in the interior exhibit smaller average librational amplitudes than those of generation 3.

1. Introduction

Dendrimers are a subclass of hyperbranched polymers, distinguished by a well-defined molecular composition which results from a repetitive sequence of synthetic steps.[1] In contrast to conventional synthetic polymers, dendrimers can be synthesized as nanoscale, almost monodisperse, materials capable of forming compact, highly symmetric three-dimensional structures with extensive, tailorable chemical functionality. These properties have answered many long-standing needs in the fields of nanochemistry, pharmacology, and surface science.[2] Much fundamental experimental characterization and theoretical analysis of dendritic structure have been conducted on polyamidoamine (PAMAM) dendrimers.[3] In these materials, the number of terminal groups doubles with each succeeding reaction step of divergent synthesis,[1] alternating between carboxyl and amine groups. Materials made from an odd number of steps, terminated with carboxyl groups, are assigned half-integer generation numbers, while materials made from an even number of steps, terminated with amine groups, are assigned integer generation numbers. For example, the generation $G = 3$ dendrimer made from an ethylenediamine core has 32 terminal amino groups. Typical representatives of PAMAM family are the β-alanine dendrimers studied in this work. Their chemical structure is illustrated in Figure 1.

These dendrimers show polydispersity of 1.0003−1.0005, which is exceptionally low even for polymers of their class. The presence of many chain ends and branched architecture allows for extremely high reactivity, solubility, and miscibility together with low intrinsic viscosity.[4] Their solution properties,[5] as well as rheological[6] and glass transition[4] behavior, suggest that open structures characteristic of low-generation materials give way to a more compact, spherical shape, beginning with generation 3.

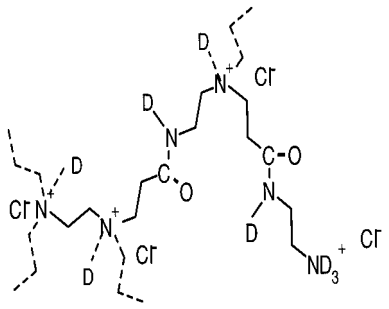

Figure 1. PAMAM branch (one of 8 for $G = 1$) showing deuteration at specific secondary amide and interior and surface tertiary amine sites.

Relatively complex constituents and precise synthesis make PAMAM dendrimers good models for studying intramolecular processes in biological polymers and for developing a theory of the growth, structure, and dynamics of dendritic polymers as a class. The amide connectivity of the dendrimer interior stabilizes the structure by hydrogen bonding, a phenomenon found also to be important for protein folding.[7] Many suggested applications rely on PAMAM's biocompatibily. These include drug delivery systems,[8,9] sequestering,[10] MRI contrasting agents,[11] and surface modifiers.[12] Correlations between the structure and mobility of PAMAM dendrimers[13−17] and their useful properties[8−12] are therefore of great interest. Many practical applications would be significantly enhanced by a more precise understanding of the dendrimer interior and surface architecture, the extent of chain back-folding, and the degree of interpenetration between neighboring molecules. While significant recent progress has been made

† Department of Applied Science.
‡ Department of Physics.
* To whom correspondence should be addressed. e-mail: rlv@nmr.physics.wm.edu.

10.1021/ma9916178 CCC: $19.00
Published on Web 01/27/2000

in this regard,[1,2] the field still lacks a complete picture of dendrimer behavior.

Several somewhat contradictory theoretical models of dendrimer structure and growth have been proposed. The kinetic model[18] predicts that during each polymerization step all generations of the dendrimer molecules remain open so that reactive terminating groups can be found both on the polymer surface and in the interior. As a result, dendrimers have a fractal structure and do not form a rigid shell at the surface.[18] According to the competing self-consistent field model,[19] the ideal "starburst" growth of the dendrimer can proceed without termini folding back, but only for a limited number of generations. This number depends on the length of the polymer spacer (distance between branching sites) and its flexibility. For PAMAM, for instance, the model predicts the possibility of starburst growth up to generations 8−10. The estimation of the moment of inertia from molecular dynamics simulations[15] has indicated that the shape symmetry changes from hemispherical to spherical with growing generation number. This supports yet another picture of dendrimers: open structures for low generations, the formation of the surface layers around generations 3−4, and a transition to globular shapes (with extensive channeling and perhaps voids in the interior) for higher generations.

Substantial experimental evidence has been accumulated which supports the existence of a structural change to a spherical shape.[13−15,17,20−24] The results of molecular dynamics simulations are supported by experimental studies of NMR relaxation of small guest molecules in dendrimer solutions.[15] Recent small-angle neutron (SANS)[16] and small-angle X-ray scattering (SAXS)[17] investigations and photoinduced electron-transfer experiments[20] also confirmed these simulations. Together with counterion mirroring,[25] these studies suggest extended dendron configurations for dendrimers in solution. For generation 7−10 polyamidoamine dendrimers SAXS exhibited features characteristic of nearly monodisperse, spherical particles with uniform internal segment densities and much higher regularity than for dilute hyperbranched polymer solutions.[17] For the lower generations, an accurate determination of particle shape and internal density distribution was not possible due to absence of higher order scattering features.

Although direct spectroscopic measurements of dendrimer structures are complicated by the lack of long-range order, much indirect information has been gained by monitoring the mobility of metal complexes incorporated in the dendrimer interior and surface.[21,22] This provides evidence of an open structure for low generations and a more compact architecture for high-generation dendrimers consistent with a change in dendrimer surface morphology around generation 3.[21,22]

To further characterize the nature of the dendrimer surface and interior, liquid state ^{13}C and ^{2}H NMR studies of dendrimer relaxation were performed.[13,14] These studies indicate that with growing generation number there is an increase in mobility at the surface and decrease of motion in the interior. This was considered evidence of extensive back-folding and the absence of a rigid surface shell.

Before now all experimental NMR work on PAMAM dendrimers has been done in solution where solvent interactions and overall molecular reorientation complicate the interpretation of structure and motion. While most proposed applications involve dendrimers in solution, solid state studies may provide valuable insight into intrinsic PAMAM structure and dynamics, resolve theoretical ambiguities, and lead to development of new applications. In this paper we present temperature- and generation-dependent quadrupole echo (QE) spectra of deuterated PAMAM ammonium chloride dendrimer salts. Line shape analysis provides information on the distribution of hydrogen bond lengths between the dendrimer spacers at secondary amide sites and at deuterated tertiary amine branching sites. Both flexible structural units and stabilizing amide connectivity with counterion attraction govern PAMAM transition from interpenetrated extended structures for low generations to a more symmetric back-folded architecture for high generations. In the course of this transition it was possible to explicitly investigate the balance between the destabilizing effects of planar intramolecular spacer motion, cone libration of terminal groups, and stabilizing effects of hydrogen bonding. This is the first use of ^{2}H NMR to characterize structure and hydrogen bonding in solid PAMAM dendrimers as a function of temperature and generation.

2. Experimental Methods

Material Preparation. Amine-terminated Starburst dendrimers (diamine core) of generations 1−3 were obtained from Aldrich as 5 g of 20 wt % solutions in methyl alcohol. Generations 5, 7, and 9 were synthesized as 0.8 g of 15−25 wt % methanol solutions and kindly donated for experiments by Dendritech Inc. (Michigan Molecular Institute). All samples were stored in a refrigerator when not in use.

Two samples of deuterated polyamidoammonium chloride salts were prepared for generations $G = 1$, 2, 3, 5, 7, and 9. Deuteration of each sample was done in four steps: (1) 2 mL of HCl and 2 mL of D_2O were added to the methanol solution; (2) the sample was dried under nitrogen at 60 °C for 24 h; (3) 2 mL of D_2O was added and step 2 repeated; (4) step 3 was repeated, and the sample was dried under vacuum at 20 °C for 3 days (with the solvent trap cleaned every 3−5 h). Theoretically, 97−99% deuteration should be achieved. The use of a strong acid results in deuteration of all secondary amide, R_2ND, and terminal ammonium, RND_3^+, sites and at least partial deuteration of tertiary amine sites,[26] R_3ND^+. Stoichiometric ratios R_2ND:RND_3^+:R_3ND^+ are $2{:}1{:}(1-2^{-G-1})^{-1}$ according to the structure illustrated in Figure 1. Dry dendrimers were powdered, packed into 5 mm outer diameter Wilmad glass sample tubes, and sealed in a glovebag under nitrogen to avoid moisture. Sealed tubes containing approximately 200 mg of sample were stored at ambient temperature. The same procedure was followed in preparation of two brominated samples for $G = 2$ with HCl replaced by DBr 47 wt % solution in D_2O bought from Aldrich Chemical Co.

Measurements. NMR experiments were conducted on a home-built spectrometer based on a 7 T superconducting magnet, using a 5 mm broad-band probe tuned to deuteron resonance at 46.06 MHz. Elevated temperatures were attained by flowing heated air around the sample coil, and low temperatures were attained using nitrogen gas cooled from a boil-off dewar. The temperature was controlled to ±0.01 °C by a LakeShore temperature controller (model DRC91-CA), with a 10 kΩ platinum sensing resistor placed close to the sample coil. For all quadrupole echo experiments the standard pulse sequence $90x-40\ \mu s-90y-\tau-$ACQ was used, accumulating 10 000 transients of 1024 complex data points. The 90° pulse length was 1.6 μs, resulting in adequate coverage over the spectral width ±200 kHz. Comparison of room temperature spectra obtained with recycle delays of 5 and 20 s indicated that a 5 s recycle delay is adequate for essentially complete relaxation of all spectral features. At elevated temperatures the relaxation was faster. Below room temperature, the 5 s relaxation delay (needed to preserve reasonable data accumulation time) might result in incomplete, frequency

dependent relaxation and consequent anisotropic deviation of apparent line intensities from stoichiometric expectations. Temperature dependent transverse relaxation effects might also cause such distortions, but this is not a serious source of error in the spectra analyzed in this paper. Ambient temperature spectra for G5 dendrimers repeated with a 20 μs delay were superimposable on those obtained with a 40 μs pulse spacing. Thus, to avoid unnecessary electronic overload of the preamplifier, a 40 μs interpulse delay τ was used for all spectra presented here. The relative errors in total intensity of different spectra due to electronic instabilities over the 24 h acquisition period were estimated to be less than 5%.

Spectra of all dendrimer generations consist of broad, overlapping powder patterns arising from three types of deuterons in rigid environments, plus two peaks in the center originating from more mobile parts of the sample. Spectral assignments are based on literature values of quadrupole coupling parameters for deuterons bonded to nitrogens in different hybridization states,[27−32] confirmed by experiment on the $G = 2$ dendrimer in which Cl^- counterions were substituted with Br^-.

Data Processing. Data manipulation was performed on Indigo2 and O2 Silicon Graphics workstations using the commercially available data visualization package PV-WAVE. Exponential apodization, corresponding to 500 Hz Lorentzian broadening, was applied to the time domain signals. The data were then left shifted, by spline interpolated fractions of a dwell time if necessary, so that a point occurred precisely at the top of the echo. This procedure is less prone to introduction of baseline artifacts than the alternative of linear phase correction after Fourier transformation. A frequency independent phase correction of 5−15° was used to minimize the signal in the out-of-phase channel. The relatively small residual asymmetry in the Fourier transformed spectra probably arises from instrumental artifacts not fully eliminated by phase cycling.

3. Theory and Spectral Simulation

Simulations. Line shapes were simulated using the SUMS algorithm,[33] in which frequency domain spectra are efficiently computed by summing sets of axially symmetric subspectra. Broadened line shapes were modeled by expressing both the quadrupole coupling constant, $\chi = (e^2 q_{zz} Q/h)$, and the asymmetry parameter of the electric field gradient tensor, $\eta = (q_{xx} - q_{yy})/q_{zz}$, in terms of a single, model dependent parameter κ which was assumed to have a Gaussian distribution, $G(\kappa)$. The explicit relation between κ and quadrupole coupling parameters corresponds to different motional models, as described later in the paper. Thus, normalized line shapes $I(\nu)$ were computed from the expressions

$$I(\nu) = p(\nu)\, f(\nu) \sum_i S(\chi(\kappa_i),\eta(\kappa_i),\nu) G(\kappa_i) \Delta\chi \qquad (1a)$$

$$G(\kappa) = N^{-1} \exp[-(\kappa - \langle\kappa\rangle^2)/2\sigma_\kappa] \qquad (1b)$$

$$N = \int_\chi G(\kappa(\chi))\, \mathrm{d}\chi \qquad (1c)$$

$$p(\nu) = \frac{\sin^3\left(\frac{\pi}{2}\sqrt{1 + 4\nu^2\, t_{90}{}^2}\right)}{\sqrt{(1 + 4\nu^2\, t_{90}{}^2)^3}} \qquad (1d)$$

$$f(\nu) = \frac{1}{1 + Q^2 \frac{(\nu - \nu_0)^2}{\nu_0{}^2}} \qquad (1e)$$

where $\Delta\chi$ is increment of χ, t_{90} is the length of the 90° pulse, ν_0 is the deuteron Larmor frequency, 46.06 MHz, Q is the probe quality factor, and $S(\chi,\eta,\nu)$ is the SUMS formula[33] for a powder pattern for the specified values χ and η. Each value of the summation index in eq 1a refers to a subspectrum defined in the SUMS algorithm. The function $p(\nu)$ corrects the simulated line shape for effects of finite pulses,[34] and $f(\nu)$ accounts for the finite bandwidth of the probe. The functional form of $f(\nu)$ corresponds to a Lorentzian response function, with full width at half-height equal to ν_0/Q. Both corrections are needed to achieve adequate fits to the experimental line shapes at frequencies $|\nu - \nu_0| \geq 100$ kHz. For example, at 100 kHz away from the center of the powder patterns, $p(\nu) = 0.84$ for the 1.6 μs 90° pulses used in our experiments, and $f(\nu) = 0.83$ for $Q = 105$. The probe Q value of 105, which was used in all the simulations of dendrimer spectra, was determined by fitting to an experimental powder pattern of a deuterated polyethylene test sample.

Equation 1a requires that successive values of κ correspond to equal increments of the quadrupole coupling constant, $\Delta\chi$. This increment was set equal to the frequency step between successive points in the experimental spectrum, because this facilitates computing the line shape with a sufficiently accurate weighting function to permit comparison with the experimental spectrum. The model dependent expressions for $\chi(\kappa)$ were inverted to obtain explicit expressions for $\kappa(\chi)$, which were then used with visual estimates of the average quadrupole coupling parameters, $\langle\chi\rangle$ and $\langle\eta\rangle$, to determine $\bar{\kappa}$, the centroid of a Gaussian distribution in κ. Normalized line shapes for each type of deuteron were computed using trial values of the distribution width. Weighted sums of these line shapes were compared with experimental spectra, and the distribution width and relative weights for each type of deuteron were adjusted by trial and error to achieve the minimum mean-square deviation between the weighted sum and experimental line shapes.

The final line shape intensity distribution should reflect the peculiarities of the skewed distribution, $G(\kappa(\chi))$, as determined by the functional relation $\chi(\kappa)$. In principle, comparison of simulated line shapes to experimental results should provide tests of the different models. In practice, wider distributions allow for better distinction, because as shown in Figure 2, the differences in skew are then more pronounced. The selection of a particular model based on only slightly broadened line shapes is likely to be ambiguous.

Models. Four models were explored. In model I, a simple Gaussian distribution of quadrupole coupling constants is assumed, i.e., $\kappa = \chi$ (solid lines in Figure 2). In this case, the first guess for the distribution width can be taken as the apparent half-width of the powder pattern horn, and its centroid is simply $\langle\chi\rangle$. Though simple and straightforward, this model can only express the presence of a distribution without reference to its physical origin. More realistic models II, III, and IV associate the distribution with hydrogen bond length, libration in a cone, and libration on a planar arc, respectively.

Hydrogen Bonding (*Model II*). For this model the parameter κ is taken to be r, the distance from the deuteron to the X-acceptor atom in a N−D···X hydrogen bond, where X can be oxygen, chlorine, or bromine anion in the case of PAMAM. The quadrupole coupling constant is related to hydrogen bond distance by the empirical expression

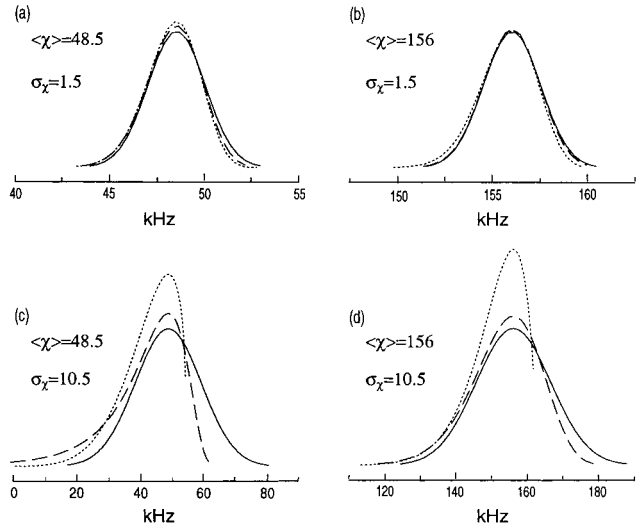

Figure 2. Normalized distributions of quadrupole coupling constants. $\langle\chi\rangle = 48.5$ kHz corresponds to RND_3^+ deuterons and $\langle\chi\rangle = 156$ kHz to R_3ND^+ deuterons. Gaussian distribution of χ in model I (solid lines), Gaussian distribution of hydrogen bond lengths in model II (dashed lines), Gaussian distribution of cone angles in model III (a and c, dotted lines), or arc lengths in model IV (b and d, dotted lines). Note that the nonlinear relation between χ and the bond lengths or angles for models II, III, and IV leads to skewed distributions, especially for wide distributions as illustrated by (c) and (d).

$$\chi_{PAS} = A - \frac{B}{r^3} \qquad (2)$$

where A and B are given in kilohertz and r in angstroms. This model makes no reference to the asymmetry parameter.[31,32,35] The nonlinear relation between r and χ implies that a Gaussian distribution in r produces the skewed distribution in χ shown as long dashed lines in Figure 2.

The constants A and B are believed to be related to the state of orbital hybridization of hydrogen donor and acceptor atoms, respectively.[32,35] For tetrahedrally bonded nitrogen, $RND_3^+\cdots Cl^-$, $A = 239$ and $B = 728$ are rather well-established[31] values (solid line fit in Figure 3a), and for the purpose of simulations we adopted them for $R_3ND^+\cdots Cl^-$. For secondary amides, $R_2ND\cdots O$, there is less agreement in the literature. Some authors interpret data using $A = 282$.[29,30] This intercept value was found to be valid for $RND_2\cdots O$ groups,[31,36−39] as illustrated in Figure 3d, but attempts[40] to refine the correlation of eq 2 for secondary amide deuterons by including corrections for nonlinear hydrogen bonds were not very successful. It must be noted in this regard that quadrupole coupling constants determined indirectly from relaxation measurements in solution, assuming a zero asymmetry parameter, are likely to be significantly different from the principal axis values required by eq 2. Long relaxation times and limited sensitivity have precluded extensive accumulation of reliable solid state quadrupole coupling parameters of secondary amides with known structures. Nevertheless, if we assume that the slope, B, is still determined by the oxygen-acceptor atom, we can conclude on the basis of a few reports[29,30] that a more appropriate intercept would be $A = 260$, as illustrated in Figure 3c.

The value $B = 572$ for oxygen is well established by the data for $RND_3^+\cdots O$[31,32] (Figure 3b) and for $RND_2\cdots O$[31,36−39] (Figure 3d). The fact that a few outlying points from the $RND_3^+\cdots O$ line come close to the

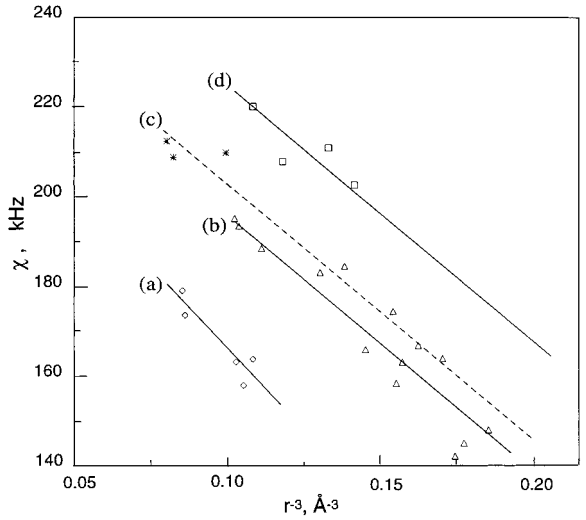

Figure 3. Dependence of quadrupole coupling constant, χ, on the inverse cube of the Y···X hydrogen bonding length, r. Points are experimental data: $Y = ND^+$, $X = Cl^-$[31] (diamonds), $Y = ND^+$, $X = O$[31,32] (triangles), $Y = RND_2$, $X = O$[31,36−39] (squares), $Y = R_2ND$, $X = O$[29,30] (stars). Lines are linear fits with intercept and slope: (a) $A = 239$, $B = 728$;[31] (b) $A = 253$, $B = 572$[32]; (c) $A = 260$, $B = 572$; (d) $A = 282$, $B = 572$.[31] In (c), the best fit A was found with the slope fixed at 572 as described in the text.

secondary amide line (Figure 3c) may indicate some as yet poorly understood differences among zwitterionic RND_3^+ deuterons. Note also that for these deuterons the best fit intercept $A = 253$ is very different from $A = 239$ (Figure 3a) found for ionic solids,[31,32] even though the nitrogen donors are tetrahedrally hybridized in both cases. In view of these limitations, it would be unwise to place much credence in quantitative values of hydrogen bond length obtained by applying eq 2 to materials of unknown structure. Nevertheless, numbers obtained in this fashion may reveal interesting and useful trends.

Fast Libration (*Models III and IV*). Averaging of observed quadrupole coupling parameters due to fast motion can be described using irreducible spherical tensors.[41] In the principal axes system (PAS) of the electric field gradient tensor, the quadrupole coupling constant and asymmetry parameter define the constant tensor elements:

$$T_0^{(2)}(\mathrm{PAS}) = \frac{\sqrt{6}}{4}\chi_{PAS}; \quad T_{\pm1}^{(2)}(\mathrm{PAS}) = 0; \quad T_{\pm2}^{(2)}(\mathrm{PAS}) = \frac{1}{4}\chi_{PAS}\eta_{PAS} \qquad (3)$$

These quantities are related to their counterparts in laboratory-fixed coordinates by a series of Euler rotations. Thus, if $\Omega_{PM}(\alpha_{PM},\beta_{PM},\gamma_{PM})$ denotes a transformation which rotates the PAS frame onto a set of molecule-fixed axes, $\Omega_{MC}(\alpha_{MC},\beta_{MC},\gamma_{MC})$ denotes a rotation from molecule-fixed axes to a crystal-fixed frame, and $\Omega_{CL}(\alpha_{CL},\beta_{CL},\gamma_{CL})$ denotes a rotation from crystal-fixed axes to laboratory-fixed axes, the tensor elements in the laboratory frame are given by

$$T_m^{(2)}(\mathrm{LAB}) = \sum_{a=-2}^{2} D_{am}^{(2)}(\Omega_{CL}) \sum_{b=-2}^{2} D_{ba}^{(2)}(\Omega_{MC}) \sum_{c=-2}^{2} D_{cb}^{(2)}(\Omega_{PM}) T_c^{(2)}(\mathrm{PAS}) \qquad (4)$$

Here, $D_{jk}^{(2)}(\Omega)$ is the j,k element of the second rank

Wigner rotation matrix for the transformation Ω. To calculate the equilibrium spectrum, $T_0^{(2)}$(LAB) must be averaged over fast motions. The time-independent Euler transformation Ω_{CL} defines the crystallite orientation in a powder sample, while both remaining transformations are time-dependent due to molecular motion. Assuming that it is permissible to average these motions independently, the averaged tensor element in the LAB system is given by

$$\langle T_0^{(2)}(\mathrm{LAB})\rangle = \sum_{a=-2}^{2} D_{am}^{(2)}(\Omega_{CL}) \sum_{b=-2}^{2} \langle D_{ba}^{(2)}(\Omega_{MC})\rangle \sum_{c=-2}^{2} \langle D_{cb}^{(2)}(\Omega_{PM})\rangle T_c^{(2)}(\mathrm{PAS}) \equiv \frac{\sqrt{6}}{8}\langle\chi\rangle(3\cos^2\beta_{CL} - 1 + \langle\eta\rangle \sin^2\beta_{CL}\cos^2\alpha_{CL}) \quad (5)$$

$$\langle D_{ij}^{(2)}(\Omega)\rangle = \int_\Omega D_{ij}^{(2)}(\Omega)\, P(\Omega)\, d\Omega$$

where angular brackets mean ensemble average due to molecular motion, $\langle\chi\rangle$ and $\langle\eta\rangle$ are observed average quadrupole coupling parameters, and $P(\Omega)$ is the model-dependent probability of orientation Ω. For model III, fast rotation about a 3-fold symmetry axis is combined with isotropic libration of the axis in a cone. Here integration over Ω_{PM}, with constant probability $^1/_3$, ensures that the average asymmetry parameter is zero. Integration over Ω_{MC} with uniform probability $[4\pi(1 - \cos\beta_{MC})]^{-1}$ gives the average quadrupole coupling constant,

$$\langle\chi\rangle = \chi_{PAS}\, {}^1/_4(3\cos^2\beta_{PM} - 1)\cos\beta_{MC}\,(1 + \cos\beta_{MC}) \quad (6)$$

Here, β_{PM} is the angle between the *Z*-axes of the PAS frame and the 3-fold rotation axis, and β_{MC} is the half-angle of the cone. For this model, inversion of eq 6 yields the following expression,

$$\bar{k} = \beta_{MC} = \cos^{-1}\left(-\frac{1}{2} + \sqrt{\frac{1}{4} + 2\,\frac{\langle\chi\rangle}{\frac{1}{2}\chi_{PAS}(3\cos^2\beta_{PM} - 1)}}\right) \quad (7)$$

Model III is appropriate for ND_3^+ deuterons, although additional considerations are needed to account for the observation of nonzero asymmetry parameters.

For $R_3ND^+\cdots Cl^-$ and $R_2ND\cdots O$ deuterons large-amplitude motion is prohibited by steric constraints. Restricted libration in a plane (model IV) is a plausible type of motion for these groups.[30] For such motion it can be assumed, without loss of generality, that the crystal- and molecule-fixed frames coincide. The transformation $\Omega_{MC}(\alpha_{MC},\beta_{MC},\gamma_{MC})$ in eq 4 reduces to the identity operator, collapsing the sum over index *b*. The largest component of the EFG tensor, q_{zz}, is coincident with the N−D bond axis to a high degree of approximation.[29,30] Following Usha et al., we assume that libration occurs in a plane containing the N−D bond perpendicular to q_{yy}, such that q_{yy} remains invariant. The libration is then defined by $\kappa = \beta_{PM}$. The transformation $\Omega_{PM}(\alpha_{PM},\beta_{PM},\gamma_{PM}) = \Omega_{PM}(0,\phi(t),0)$, and effects of libration on the observed quadrupole coupling parameters are easy to evaluate by averaging eq 5 over the interval $-\phi_0 \le \phi \le \phi_0$ with uniform probability $(2\phi_0)^{-1}$. This procedure gives the following expressions for the average quadrupole coupling constant and a motionally induced asymmetry parameter:

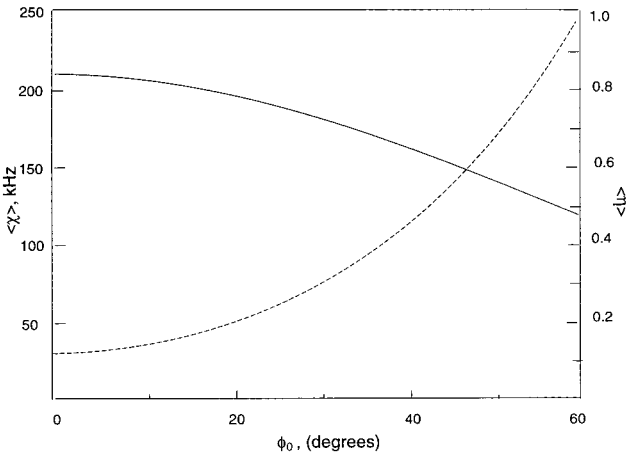

Figure 4. Average quadrupole coupling constant, $\langle\chi\rangle$ (solid line), and asymmetry parameter, $\langle\eta\rangle$ (dashed line), dependence on libration amplitude for the planar libration of N−D bond (see eq 8) with $\chi_{PAS} = 210$ kHz and $\eta_{PAS} = 0.12$.

$$\langle\chi\rangle = 0.5\chi_{PAS}[(1 - \langle c^2\rangle)(1 - \eta_{PAS}) - 2\langle c^2\rangle] \quad (8a)$$

$$\langle\eta\rangle = \frac{3(\langle c^2\rangle - 1) - \eta_{PAS}(\langle c^2\rangle + 1)}{(1 - \langle c^2\rangle)(1 - \eta_{PAS}) - 2\langle c^2\rangle} \quad (8b)$$

$$\langle c^2\rangle = \frac{1}{2}\left(1 + \frac{\sin 2\phi_0}{2\phi_0}\right) \quad (8c)$$

Here, $\langle c^2\rangle$ is the ensemble average of $\cos^2\phi(t)$. To ensure freedom from algebraic errors which can plague this sort of calculation, we checked that identical answers are obtained using Cartesian tensors and 3 × 3 orthogonal Euler rotation matrices.[42] As expected, $\langle\chi\rangle$ decreases and $\langle\eta\rangle$ increases with increasing libration amplitude, as illustrated in Figure 4. The mean of a Gaussian distribution of $\kappa = \phi_0$ can be determined by choosing a plausible value for η_{PAS}, such that numerical inversion of eq 8b reproduces the experimentally observed value for $\langle\eta\rangle$. Then χ_{PAS} can be estimated from eq 8a using the observed $\langle\chi\rangle$. Finally, eq 2 may then be solved to determine the average hydrogen bond length.

Effects of libration on the hydrogen bond length derived from model I can be accounted for by replacing *A* and *B* in eq 2 by their "motionally reduced" equivalents *AF* and *BF*, where the factor $F = \langle\chi\rangle/\chi_{PAS}$ is determined from eq 6 or 8a for libration in a cone or in a plane, respectively. This approximate procedure ignores the distribution of libration amplitudes. It effectively reduces both the centroid and the width of the χ_{PAS} distribution ascribed to the hydrogen bond length. If no librational corrections are applied, the derived values of σ_r and $\bar{r}$ for hydrogen bonding will be slightly underestimated.

The errors in model dependent parameters reported in this paper were calculated by standard error propagation methods starting from estimated uncertainties for the observables. The absolute error for the amplitude of cone libration, $\Delta\beta_c$, was found to be less than 5°. Uncertainties in the χ_{PAS} values are equal to the corresponding experimental errors in the average quad-

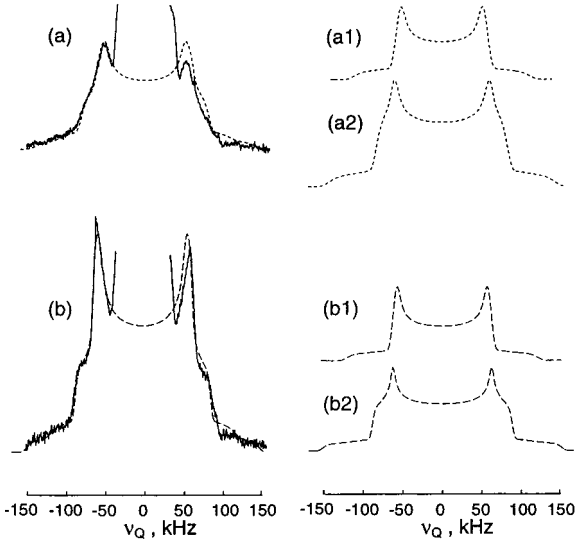

Figure 5. Experimental spectra (solid lines) and fits (dashed lines) assuming Gaussian distributions of hydrogen bond length with averaging due to planar librations of the dendrimer spacer for underlying powder patters of (a) brominated and (b) chlorinated $G = 2$ dendrimers at −30 °C. Insets show the separate powder patterns whose sum best fits the experimental data. (a1) fit for $RND_3^+\cdots Br^-$, $\langle\chi\rangle = 149 \pm 2$ kHz, $\langle\eta\rangle = 0.07 \pm 0.01$, $\sigma_r = 0.074 \pm 0.02$ Å, integrated intensity = 1.0 ± 0.1, $\eta_{PAS} = 0.05$, $\chi_{PAS} = 152 \pm 3$ kHz, $\phi_0 = 11 \pm 4°$, $\bar{r} = 2.03 \pm 0.06$ Å; (a2) fit for R_2ND, $\langle\chi\rangle = 192 \pm 2$ kHz, $\langle\eta\rangle = 0.16 \pm 0.01$, $\sigma_r = 0.12 \pm 0.02$ Å, integrated intensity = 2.0 ± 0.4, $\eta_{PAS} = 0.12$, $\chi_{PAS} = 199 \pm 3$ kHz, $\phi_0 = 15 \pm 4°$, $\bar{r} = 2.1 \pm 0.1$ Å; (b1) fit for $RND_3^+\cdots Cl^-$, $\langle\chi\rangle = 161 \pm 2$ kHz, $\langle\eta\rangle = 0.05 \pm 0.01$, $\sigma_r = 0.07 \pm 0.02$ Å, integrated intensity = 1.0 ± 0.1, $\eta_{PAS} = 0.05$, $\chi_{PAS} = 161 \pm 3$ kHz, $\phi_0 = 1 \pm 1°$, $\bar{r} = 2.11 \pm 0.03$ Å; (b2) fit for R_2ND, $\langle\chi\rangle = 201 \pm 2$ kHz, $\langle\eta\rangle = 0.17 \pm 0.01$, $\sigma_r = 0.09 \pm 0.02$ Å, integrated intensity = 1.7 ± 0.4, $\eta_{PAS} = 0.12$, $\chi_{PAS} = 210 \pm 3$ kHz, $\phi_0 = 17 \pm 2°$, $\bar{r} = 2.25 \pm 0.1$ Å.

rupole coupling constants measured from the spectra. The uncertainty in the amplitude of planar libration grows with decreasing angle, ϕ_0. The uncertainty in the average hydrogen bonding length, Δr, is determined mainly by the planar libration amplitude and is higher for larger ϕ_0.

4. Results and Discussion

On the basis of literature values of quadrupole coupling parameters for similar materials,[27−32] the two widest powder patterns, which are observed for all generations, are assigned to secondary amide and protonated tertiary amine deuterons, respectively. Deuteration of tertiary amine sites was ensured during our preparation procedure by the excess of strong acid and confirmed by measurements conducted on generation 2 dendrimers with counterion substitution. Substitution of Br^- (Figure 5a) for Cl^- (Figure 5b) resulted in a noticeable decrease of χ for deuterons at both the branching amine and amide sites, from 161 (Figure 5b1) to 149 (Figure 5a1) and 201 (Figure 5b2) to 192 kHz (Figure 5a2), respectively. The observed changes for deuterons in the dendrimer interior demonstrate that the anions are not confined to the dendrimer surface.

Typical experimental spectra, calculated line shapes, and their difference for the two widest powder patterns of the generation 7 dendrimer at room temperature are shown in Figure 6. The best fit quadrupole coupling parameters were found to be the same for all four models: for the widest pattern $\langle\chi\rangle = 203 \pm 2$ kHz and $\langle\eta\rangle = 0.13 \pm 0.01$, and $\langle\chi\rangle = 156 \pm 2$ kHz and $\langle\eta\rangle = 0.09$ ± 0.01 for the narrower one. The best fit distribution widths for the wide and narrow patterns of different models are $\sigma_\chi = 10.7$ kHz and 10.5 kHz (model I, Figure 6a), $\sigma_r = 0.12$ and 0.09 Å (model II, Figure 6b), $\sigma_\beta = 10°$ and 9° (model III, Figure 6c), and $\sigma_\phi = 7.5°$ and 7° (model IV, Figure 6d), respectively. The distributions of hydrogen bond length were calculated including the effects of planar libration as described above.

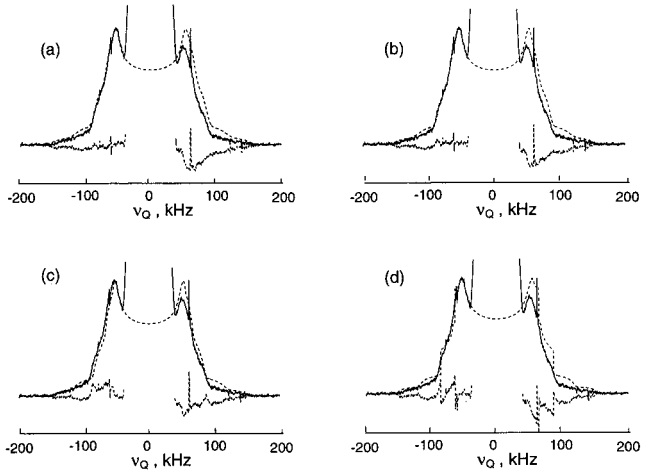

Figure 6. Experimental (solid lines) and simulated (dashed lines) powder patterns for $G = 7$ dendrimer at ambient temperature (24 °C). Differences between simulations and experiments are shown as dotted lines. All spectra here were simulated with two overlapping powder patterns: $\langle\chi\rangle = 203$ kHz with $\langle\eta\rangle = 0.13$ and $\langle\chi\rangle = 156$ kHz with $\langle\eta\rangle = 0.09$, respectively. In (a), Gaussian distributions of χ (model I) were assumed, with $\sigma_\chi = 10.7$ and 10.5 kHz for the R_2ND and R_3ND^+ powder patterns, respectively. In (b), Gaussian distributions of hydrogen bond length (model II) were used with $\sigma_r = 0.12$ and 0.09 Å. In (c), libration in a cone (model III) was used with $\sigma_\beta = 10°$ and 9°, and in (d), libration on an arc (model IV) was characterized by $\sigma_\phi = 7.5°$ and 7°.

It is noteworthy that, compared with a symmetric distribution of χ values, both librational and hydrogen bond length distributions are biased toward the lower frequencies (Figure 2, short and long dashed lines), while for wide distributions the librational models require a cutoff at high frequencies. This gives the higher frequencies greater weight and produces characteristic features in the line shapes (Figure 6c,d), which are not present in the experimental data. The fits using distributions of hydrogen bond lengths are marginally better than those using a symmetric distribution of quadrupole coupling constants. Thus, the experimental data reflect predominantly the intra-dendrimer distribution of hydrogen bond lengths. Results of fitting this model to the spectra for all samples are summarized in Table 1. In all cases the temperature dependence of the average quadrupole coupling parameters $\langle\chi\rangle$ and $\langle\eta\rangle$ was ascribed to planar libration and interpreted using eq 8. At this point in the analysis the precision of the data does not warrant introduction of a distribution of libration angles.

The small change in asymmetry parameter upon counterion substitution, from $\langle\eta\rangle = 0.17$ to 0.16 for $R_2ND\cdots O$, corresponds to a negligible decrease in librational amplitude (from 17° to 15°) of the dendrimer spacers. Larger changes in libration amplitude (from 1° to 11°) found for R_3ND^+ groups could be associated with less efficient packing around the larger anion, perhaps arising from reduced electrostatic interactions. The approximate 10 kHz decrease in $\langle\chi\rangle$ for secondary amide

Table 1. Best Fit Parameters for Three Deuterated Sites of PAMAM Dendrimer

	RND_3^+		R_3ND^+			R_2ND		
G\par	$\bar{\beta}_c$, deg	$\sigma_\beta \pm 2°$	$\bar{\phi}_0$, deg	$\sigma_r \pm 0.01$, Å	$\bar{r}$, Å	$\bar{\phi}_0$, deg	$\sigma_r \pm 0.02$, Å	$\bar{r}$, Å
G1								
RT	21 ± 5	9.0	14 ± 3	0.09	2.10 ± 0.10	16 ± 2	0.11	2.21 ± 0.07
G2								
RT	21 ± 5	9.0	16 ± 2	0.07	2.10 ± 0.10	19 ± 2	0.12	2.20 ± 0.10
recent	22 ± 5	9.0	11 ± 4	0.06	2.12 ± 0.06	19 ± 2	0.11	2.25 ± 0.10
−30 °C	16 ± 5	8.5	1 ± 1	0.07	2.11 ± 0.03	17 ± 2	0.09	2.25 ± 0.10
+45 °C	25 ± 5	10.0	11 ± 4	0.06	2.11 ± 0.06	19 ± 2	0.11	2.20 ± 0.10
G3								
RT	25 ± 3	6.0	21 ± 2	0.12	2.20 ± 0.10	19 ± 2	0.11	2.10 ± 0.10
recent	24 ± 3	6.3	18 ± 2	0.08	2.20 ± 0.10	19 ± 2	0.12	2.16 ± 0.10
−30 °C	22 ± 3	8.6	19 ± 2	0.11	2.20 ± 0.10	17 ± 2	0.10	2.20 ± 0.10
+45 °C	25 ± 3	6.3	23 ± 2	0.12	2.20 ± 0.10	23 ± 2	0.13	2.22 ± 0.12
G5								
RT	21 ± 4	10.0	14 ± 3	0.07	2.08 ± 0.08	19 ± 2	0.12	2.23 ± 0.11
recent	18 ± 4	11.0	11 ± 4	0.06	2.06 ± 0.06	20 ± 2	0.13	2.31 ± 0.11
G7								
RT	20 ± 4	10.0	16 ± 2	0.09	2.10 ± 0.10	8 ± 4	0.13	2.18 ± 0.04
recent	16 ± 4	11.5	11 ± 4	0.09	2.09 ± 0.06	15 ± 3	0.17	2.30 ± 0.10
G9								
RT	20 ± 4	10.0	11 ± 4	0.09	2.09 ± 0.06	11 ± 4	0.13	2.21 ± 0.05
recent	18 ± 4	11.5	11 ± 4	0.09	2.10 ± 0.06	15 ± 3	0.17	2.30 ± 0.10
−30 °C	16 ± 4	8.5	8 ± 4	0.11	2.11 ± 0.04	1 ± 1	0.12	2.21 ± 0.03
+45 °C	22 ± 4	10.0	11 ± 4	0.09	2.09 ± 0.06	17 ± 2	0.13	2.30 ± 0.10

sites observed upon substitution of Br^- for Cl^- is most probably caused by a decrease of hydrogen bond length. This hypothesis is supported by the fact that the decrease in average hydrogen bond length at these sites is equal to the difference in diameters between Cl^- and Br^- anions, $\Delta r = 0.14 \pm 0.02$ Å. Within experimental error, the same holds true for hydrogen bonds at protonated branching sites, for which $\Delta r = 0.09 \pm 0.04$ Å. The slightly larger changes in average hydrogen bond length found for secondary amide sites suggest greater flexibility of spacers compared to the branch points. The observed increase in powder pattern distribution widths from 7 to 10 kHz corresponds to a slightly wider distribution of hydrogen bonding environments in the brominated sample.

In simulations for the brominated sample, the *A* and *B* parameters of the quadrupole coupling−hydrogen bond relation, eq 2, were assumed to be the same as for the chlorinated G2 dendrimer $R_3ND^+\cdots Cl^-$. This is reasonable since the χ_{PAS} values for $RND_3^+\cdots Cl^-$ and $RND_3^+\cdots Br^-$ are similar,[27,28] and the hybridization symmetry is preserved upon anion substitution. The assumed values of η_{PAS}, used for quantitative estimation of libration amplitudes, require further justification. These quantities can be measured only at very low temperatures for "static" deuterons, whose long relaxation times (≥10 s) would imply prohibitively long experiments. On the basis of literature citations for secondary amide[29,30] and static ammonium[27,28,31,32] deuterons and our own measurements at −30 °C, reasonable maximum PAS values for the asymmetry parameters of R_2ND and R_3ND^+ are estimated to be 0.12 and 0.05, respectively. These values depend on the electronic environment around the dendrimer spacer, which we assume to be independent of dendrimer generation. If the assumed values of η_{PAS} are too large, the calculated libration amplitudes and hydrogen bond lengths will be underestimated, but qualitative conclusions about the observed trends will not be affected.

The narrowest powder patterns present in the spectra for all generations (Figure 7) are assigned to motionally averaged deuterons of terminal $RND_3^+\cdots Cl^-$ groups. Room temperature values of the RND_3^+ characteristic

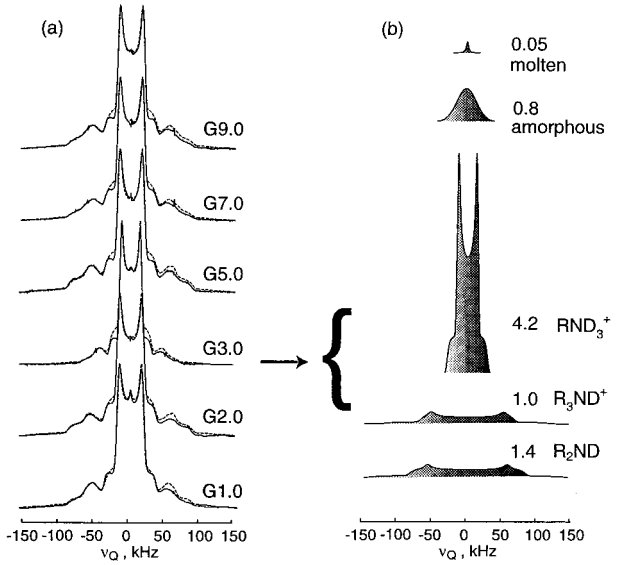

Figure 7. (a) Room temperature experimental spectra and fits for all generations studied; (b) deconvoluted fit for $G = 3$ with corresponding integrated intensities. Parameters determined from fitting these spectra are listed in Tables 1−3.

quadrupole coupling parameters, together with those for the RND_2 and R_3ND^+ powder patterns, are summarized in Table 2 and illustrated in Figure 8 (solid lines).

At ambient temperature, a minimum value of $\langle\chi\rangle$ for the R_2ND sites is found at generation 3 (Figure 8a), and smaller asymmetry parameters are observed for higher generations (Figure 8d). At R_3ND^+ sites, generation 3 shows a maximum value of both $\langle\chi\rangle$ and $\langle\eta\rangle$ (Figure 8b,e). No generation dependence is observed for the quadrupole coupling parameters of the terminal ND_3^+ groups for fresh materials studied at room temperature (the third column in Figure 8 (solid lines)): $\langle\chi\rangle = 49.0 \pm 0.05$ kHz and $\langle\eta\rangle = 0.11 \pm 0.005$. Comparing to $\langle\eta\rangle$ at −30 °C, Figure 8 (stars), it can be seen that the sign of the changes in asymmetry with growing temperature is opposite for interior and terminal groups. Deviations of the asymmetry parameters from their PAS values reflect the amplitudes of librational motion according

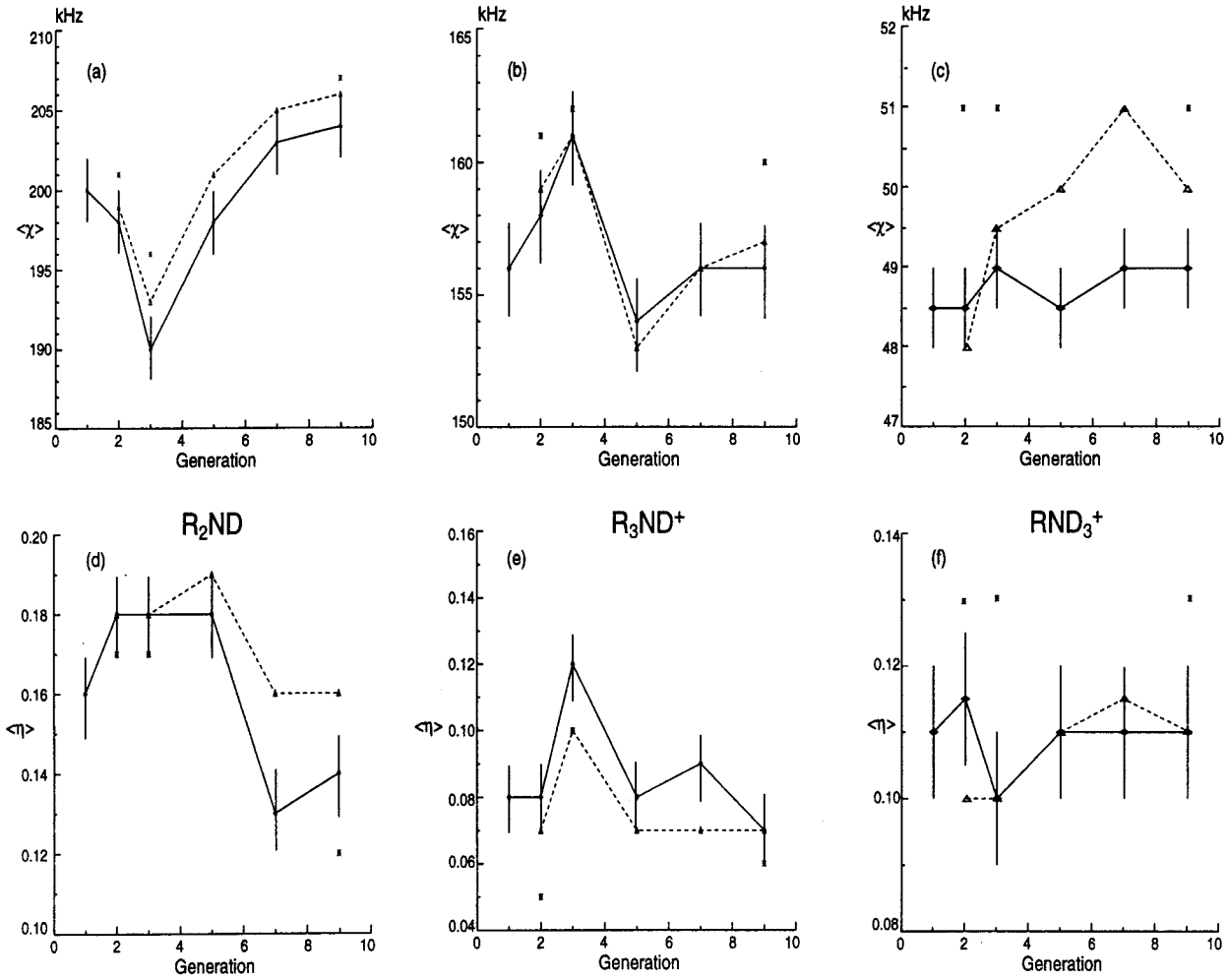

Figure 8. Generation dependence of quadrupole coupling parameters for three overlapping powder patterns: (a) and (d) R_2ND, (b) and (e) R_3ND^+, and (c) and (f) RND_3^+. Lines connecting the points are drawn to guide the eye: room temperature data for fresh samples (solid lines), data obtained at room temperature after annealing at 55 °C for 2 days (dashed lines); data at −30 °C (stars). Error bars for the points connected by solid lines also apply for the other points for the same material.

Table 2. Best Fit Quadrupole Coupling Parameters for Three Deuteron Sites of Studied PAMAM Generations, at Room Temperature

	RND_3^+			R_3ND^+			R_2ND		
G	$\langle\chi\rangle \pm 0.5$, kHz	$\sigma_\chi \pm 0.5$, kHz	$\langle\eta\rangle \pm 0.005$	$\langle\chi\rangle \pm 2$, kHz	$\sigma_\chi \pm 1$, kHz	$\langle\eta\rangle \pm 0.01$	$\langle\chi\rangle \pm 2$, kHz	$\sigma_\chi \pm 1$, kHz	$\langle\eta\rangle \pm 0.01$
G1	48.5	5.0	0.110	156	10.5	0.08	200	8	0.16
G2	48.5	5.0	0.115	157	8.0	0.09	198	9	0.18
G3	49.0	4.0	0.100	161	11.0	0.12	190	10	0.18
G5	48.5	5.0	0.110	154	8.0	0.08	198	9	0.18
G7	49.0	5.4	0.110	156	10.5	0.09	203	11	0.13
G9	49.0	5.4	0.110	156	10.5	0.07	204	10	0.14

to eq 8.[30] To measure PAS quadrupole coupling parameters, we would have to reach temperatures much lower than −30 °C, when librations would cease.

It is interesting that even though the librational amplitudes are about the same for amide sites of generations 2, 3, and 5, generation 3 has an average coupling constant, $\langle\chi\rangle = 190$ kHz, which is much smaller than the values for other generations. Simultaneously, at room temperature the tertiary amine sites of generation 3 show the smallest reduction of average quadrupole coupling constant, but they have the largest asymmetry parameter. These observations suggest that the motion of generation 3 dendrimers is different, in some as yet unspecified way, from that of the other generations.

The distribution widths for quadrupole coupling constants of RND_3^+ groups are approximately 5 kHz, roughly half of those for the other sites for which rapid 3-fold rotation is absent (see Table 2). For such narrow distributions, Figure 2a,b shows that it is hard to discriminate between libration of the 3-fold axis and hydrogen bond distances as the underlying source of the distribution.

Over the temperature range of 75 °C, $\langle\chi\rangle$ values for all sites of generations 2, 3, and 9 decrease uniformly with increasing temperature. This is accompanied by a noticeable decrease in $\langle\eta\rangle$ for RND_3^+ deuterons and an increase in $\langle\eta\rangle$ for the other sites. Typical line shapes and best fits are shown in Figure 9 for generations 2, 3, and 9 at two representative temperatures, −30 °C (Figure 9a) and +45 °C (Figure 9b). Corresponding characteristic fit parameters are listed in Tables 1, 3, and 4.

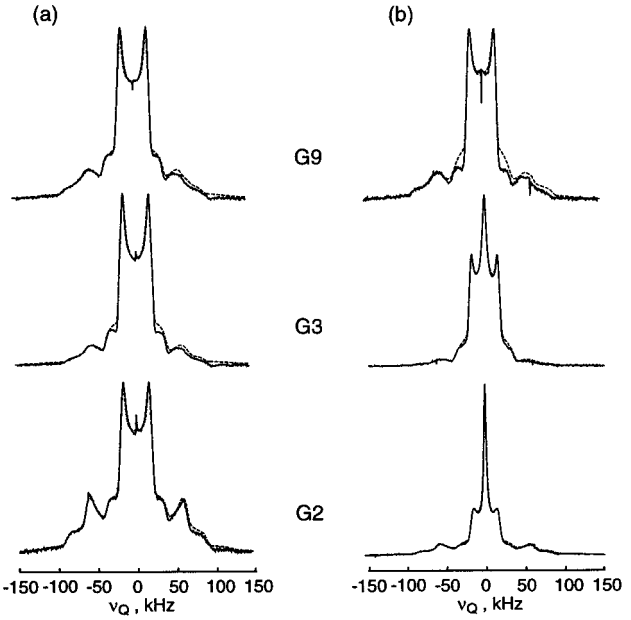

Figure 9. Experimental spectra and simulations for three PAMAM generations at −30 (a) and 45 °C (b). The characteristic fit parameters are listed in Tables 1, 3, and 4.

Table 3. Characteristic Quadrupole Coupling Parameters for Three PAMAM Generations, G2, 3, and 9, at −30 and +45 °C (See Figure 9)

	RND_3^+		R_3ND^+		R_2ND	
	$\langle\chi\rangle \pm 0.5$, kHz	$\langle\eta\rangle \pm$ 0.01	$\langle\chi\rangle \pm 2$, kHz	$\langle\eta\rangle \pm$ 0.01	$\langle\chi\rangle \pm 2$, kHz	$\langle\eta\rangle \pm$ 0.01
G2						
−30 °C	51.0	0.130	161	0.05	201	0.17
+45 °C	46.5	0.100	158	0.07	197	0.18
G3						
−30 °C	51.0	0.130	162	0.10	196	0.17
+45 °C	49.0	0.095	159	0.13	194	0.20
G9						
−30 °C	51.0	0.130	160	0.06	207	0.12
+45 °C	48.0	0.080	156	0.07	204	0.17

For amide and amine deuterons, the model of asymmetric planar libration is fully consistent with the temperature dependent data and with our observation of short relaxation times,[30] $T_{1Z} < 1$ s, for these deuterons. The best fit parameters obtained using these models are listed in Table 1.

The nonzero asymmetry parameters exhibited by RND_3^+ are inconsistent with a simple symmetric rotor picture and demonstrate the necessity for corrections to model III. Under conditions of fast motion, when rates are much higher than the static quadrupole splitting, nonzero asymmetry parameters can arise if populations for the cone "sites" used to define the ND_3^+ axis are not equal, i.e., if the probability of orientation within the cone is nonuniform. Another source of residual asymmetry is unequal populations of the sites defining 3-fold jumps of the ND_3^+ group. For two-site (planar) libration of the RND_3^+ rotation axis, the observed asymmetry parameter should increase[28] with increasing temperature. Our observation of the opposite tendency rules out this explanation. Instead, the asymmetry seems to be the result of unequal rotation and libration site populations, which implies nonuniform probabilities and nonideal geometries for motional averaging (eqs 5 and 6). Such skewed geometries may arise from one of the ammonium ND bonds orienting toward the chloride anion. The other two ammonium deuterons could be partially hydrogen bonded to carboxylic oxygens. This would cause unequal χ_{PAS} and η_{PAS} values simultaneously with unequal site populations. Then, the observed decrease in $\langle\eta\rangle$ with growing temperature could be explained simply as an increase in the symmetry of rotation and cone libration.

To avoid introducing too many independent parameters, the RND_3^+ spectra were simulated using a single, phenomenologically determined value for the motionally averaged asymmetry parameter $\langle\eta\rangle$. Distributions of $\langle\chi\rangle$ were included in the simulation as specified by model III, a Gaussian distribution of cone angles (cf. eqs 6 and 7). The angle between PAS and molecule-fixed Z axes was assumed to be $\beta_{MP} = 70.5°$,[28] and for each generation χ_{PAS} was fixed at the value derived by applying the planar libration model IV (cf. eq 8) to interior R_3ND^+ sites. We believe that χ_{PAS} values determined for interior $R_3ND^+\cdots Cl^-$ sites provide a reasonable approximation for RND_3^+ deuterons due to similarities in symmetry and hybridization states for both groups.[28,31] Within experimental error, these values turned out to be temperature independent. Quite a large difference was found between generation 3, for which χ_{PAS} is 171 ± 3 kHz, and all other generations, for which χ_{PAS} is 162 ± 3 kHz. This reflects intrinsic structural peculiarities of generation 3 and will be further discussed in terms of librational amplitudes and hydrogen bond distances.

Although the accuracy of the quantitative characterization of hydrogen-bonding length on the basis of eq 2 should be treated with caution, the numbers are reasonable, and some qualitative conclusions can be drawn. From simple geometric considerations (bond lengths[30] and angles[43]), the minimum hydrogen bond length between secondary amide deuteron and carboxylic oxygen of the same spacer can be estimated to be 2.45 Å. This is significantly larger than all the values for interior deuterons given in Table 1. Therefore, the experimental spectra reveal information about hydrogen bonding between neighboring spacers of the same or different dendrimer molecules. Although X-ray data for PAMAM model compounds are lacking, this interpretation is consistent with X-ray determination of NH···O hydrogen bond distances in other model dendrimers with amide terminal groups, for which N···O distances 2.84 ± 0.08 Å were found for intramolecular hydrogen bonds and 2.94 ± 0.05 Å for intermolecular hydrogen bonds.[44] The fact that $\bar{r}$ turns out to be essentially temperature independent for all generations provides further strong support for the validity of models II and IV. For high and low generations, the hydrogen bond length at the branching R_3ND^+ sites, $\bar{r} = 2.1$ Å, is only slightly smaller than at the spacer RND_2 sites, $\bar{r} = 2.2$ Å. The smallest difference is found for generation 3. This suggests a uniform distribution of local structures throughout the dendrimer, which is further confirmed by comparatively narrow distribution widths, $\sigma_r < 0.2$ Å. Recalling the effect of anion substitution, it is possible that equilibrium distance between RND_3^+ and anions imposes a steric constraint on the ability of secondary amide groups to participate in hydrogen bonding and thus determines the structural order for the whole dendrimer molecule. This implies that the dendrimer structure can be expected to change somewhat so as to accommodate various included materials.[15,21,22]

Librational amplitudes are equal, within experimental error, at both interior sites and are slightly larger for dendrimer termini. Therefore, in accord with the

Table 4. Fitted Relative Intensities and Stoichiometric Expectations for All Deuterated Sites, Including Parameters for the Gaussian and Lorentzian Components

	$I(RND_3^+)$:$I(R_3ND^+ + R_2ND)$		$I(R_2ND)$:$I(R_3ND^+)$		Gaussian		Lorentzian	
	stoich	fit	stoich	fit	$\nu_{1/2} \pm 1$, kHz	I, %	$\nu_{1/2} \pm 0.5$, kHz	I, %
G1	1.333	1.2 ± 0.3	2	1.0 ± 0.3	12	9 ± 5	2	1 ± 0.5
G2								
−30 °C	1.143	0.6 ± 0.3	2	1.7 ± 0.5	14	6 ± 3		0
RT	1.143	1.2 ± 0.3	2	3.4 ± 0.5	14	7 ± 3	2	0.2 ± 0.2
+45 °C	1.143	0.8 ± 0.3	2	1.5 ± 0.4	12	8 ± 4	2	21 ± 5
G3								
−30 °C	1.067	2.1 ± 0.8	2	1.2 ± 0.4	14	2 ± 1		0
RT	1.067	1.7 ± 0.7	2	1.4 ± 0.4	14	10 ± 5	2	0.6 ± 0.3
+45 °C	1.067	2.9 ± 1.2	2	1.4 ± 0.4	14	21 ± 5	3	13 ± 5
G5	1.016	1.0 ± 0.3	2	2.8 ± 0.5	14	3 ± 2	2	0.3 ± 0.2
G7	1.004	1.3 ± 0.6	2	1.2 ± 0.3	14	5 ± 3	2	0.4 ± 0.2
G9								
−30 °C	1.001	1.1 ± 0.3	2	1.0 ± 0.3	14	8 ± 4		0
RT	1.001	1.2 ± 0.3	2	1.4 ± 0.4	14	4 ± 2	2	0.3 ± 0.2
+45 °C	1.001	1.1 ± 0.3	2	2.0 ± 0.4	14	10 ± 5	2	0.4 ± 0.2

physically reasonable picture, dendrimer mobility increases from the center outward. For generations 5 and greater the librational amplitudes at interior and termini are slightly smaller, indicating more rigid or crowded structures. With the temperature increasing from −30 to +45 °C, the motional amplitudes increase at all deuterated sites (Table 1). For generation 2, the amplitude of planar libration increases more at R_3ND^+ sites (from 1° to 11°), while for generation 9 greater increase is found for the R_2ND sites (from 1° to 13°). For generation 3 the temperature dependencies of the librational amplitudes as well as their values are almost uniform throughout the dendrimer, the same being true for the hydrogen bond lengths.

Amide hydrogen bond libration is a measure of the restricted mobility of the dendrimer arms, while libration of the amine hydrogen bonds reports primarily on the motion of the counterion. Thus, the open structure of generation 2 allows thermal energy to be dissipated by increasing Cl^- mobility, while interpenetration between neighboring molecules hinders the motional freedom of the dendrimer arms. In contrast, the compact, folded structure of generation 9 spatially restricts Cl^- mobility and thermal energy preferentially increases the mobility of the dendrimer network. For generation 3, mobility and hydrogen bonding are uniform at all sites, indicating that this material most probably is neither folded nor extensively interpenetrated. Consequently, we believe that nominally identical hydrogen bond lengths between the dendrimer spacers observed for generations 1, 2, 5, 7, and 9 can be explained by interpenetration of neighboring molecules for low generations (<3) and by intramolecular back-folding for high generations (≥5). The onset of a transition, to a more symmetric, folded state at generation 3, hinders intermolecular penetration.

Adequate fits of all line shapes in the middle of the spectrum required addition of Gaussian and Lorentzian lines of different width. An increase in intensity of these components, at the expense of the three powder patterns, was observed with increasing temperature (see for $T = -30$ and +45 °C in Figure 9 and Table 4). The parameters for Gaussian and Lorentzian components as well as the stoichiometric and measured relative intensities of the three overlapping powder patterns are listed in Table 4. In most cases, simulations for generations greater than 2 yielded total intensities for interior deuteron sites that were smaller than would be expected from stoichiometry (Table 3, columns 1 and 2). These deviations could be due to incomplete deuteration.

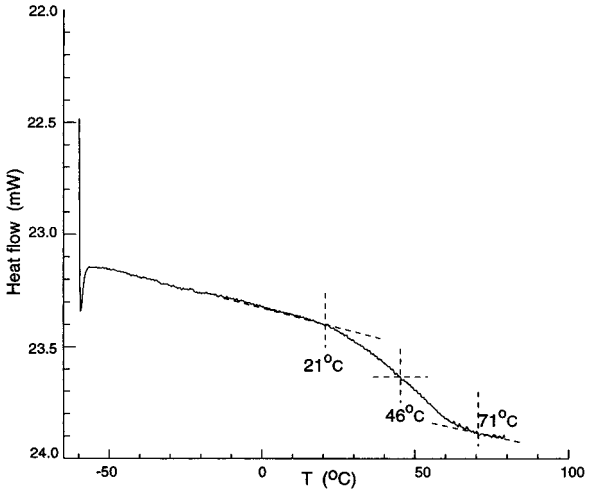

Figure 10. Differential scanning calorimetry curve for G2 deuterated PAMAM dendrimer salt. This curve was obtained on a 10 mg sample using a Perkin-Elmer Pyris-1 calorimeter, scanning from −60 to +80 °C at 10 °C/min.

It is tempting to associate the powder patterns with crystalline regions, the Gaussian component with more mobile, amorphous regions, and the narrow Lorentzian component with a small fraction of molten polymer. However, it is important to realize that wide deuteron powder patterns from rigid, polycrystalline material are not distinguishable from those of rigid, disordered amorphous material. Solid amine-terminated dendrimers are known to be entirely amorphous, with broad glass transition temperatures starting at −11 °C for G0 to 13 °C for G>4.[4] Preliminary DSC data for G2 dendrimer salts, presented in Figure 10, also reveal no evidence of a crystalline transition. Instead, the onset of a broad exothermic feature (21−71 °C) coincides with the first appearance of the Gaussian component of the deuteron line shape. The narrow Lorentzian component, which is absent in spectra obtained below room temperature, continues to grow with increasing temperature up to 65 °C, where the sample begins to flow (data not shown). We therefore associate both features with the onset of a broad glass transition. Quantitative DSC measurements are hampered by the extremely hygroscopic nature of PAMAM salts, but our NMR data demonstrate that the addition of ionic charges to the solid raises T_G by about 24 °C relative to the neutral polymers. This is qualitatively in accord with theoretical predictions.[45]

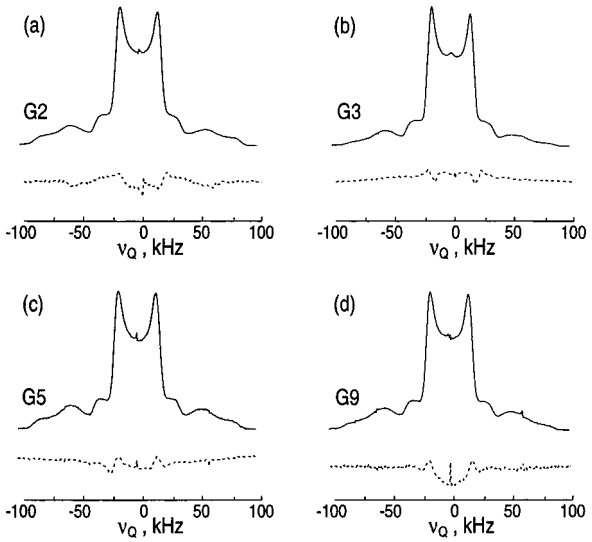

Figure 11. Powder pattern behavior after annealing at 55 °C for 2 days for generations G2 (a), G3 (b), G5 (c), and G9 (d). Solid lines are powder patterns for fresh samples. Dashed lines are difference spectra, "fresh" minus "annealed".

For all generations, the integrated intensities of both Gaussian and Lorentzian components increase with increasing temperature. For generations 2 and 9, the Gaussian component grows less than the Lorentzian component, while for generation 3 both fractions grow almost equally. The observation of two components with very different line width for material above T_G is unusual. One possible interpretation is that the narrow Lorentzian peak arises from isotropic reorientation of individual dendrimer molecules while the broader Gaussian component is associated with slower motion in locally ordered regions.

A slight temperature and time hysteresis was observed for the fractions of mobile component, which is not unusual for amorphous polymers. As can be seen from Figure 11, for annealed samples the changes in line shapes involved not only the middle of the spectra but also the overlapping powder patterns. The fraction of rigid material decreased after the samples annealed at 55 °C were cooled back to room temperature. Similar decreases progressed slowly in samples stored at ambient temperature over the period of a year. The extent of this hysteresis is clearer from the analysis of structural parameters, marked "recent" room temperature data, listed in Table 1. For high generations (>3) a slight increase in average hydrogen bond length and distribution width, together with smaller librational amplitudes of the termini, was observed after annealing. It is possible that there was sufficient thermal energy for some dendrimer arms to back-fold in the interior during the heat treatment, thus slightly decreasing voids in the interior. This would create less uniform structures and more hindrance to librational motion. However, the magnitude of the observed changes is close to experimental error, and further speculation is not warranted.

5. Conclusions

Solid state deuteron NMR data obtained for six PAMAM generations have been interpreted to develop a self-consistent and qualitatively complete picture of the dendrimer structure and fast motional amplitudes. Spectra of low- and high-generation materials exhibit the same characteristic features, which allows equally detailed characterization of all generations. This task has been problematic for other experimental methods.[16,17] Quadrupole echo spectra of interior amide and protonated tertiary amine deuterons were simulated assuming distributions of hydrogen bond lengths (model II) and motional averaging due to planar librations (model IV). The hydrogen bond length at both sites decreased with increasing anion radius. Similar quadrupole coupling and motional parameters are found for low- and high-generation dendrimers, which implies that intermolecular penetration and intramolecular back-folding both reduce dendrimer mobility. Quantitative estimation of the amplitudes of libration and hydrogen bond lengths was achieved, with a degree of accuracy reasonable for complex polymeric systems. However, the quadrupole echo line shapes provide little quantitative information about the rates of libration and rotation, other than that they are fast on the ^{2}H line shape time scale of $\sim 10^9$ s^{-1}.

Our results suggest that the lower generation PAMAM dendrimer salts appear to form a loose, network of interpenetrating neighboring molecules. This is consistent with REDOR results for benzyl ether dendrimers.[46] Some back-folding for low generations cannot be ruled out by our data, but the structure is certainly open enough to allow significant counterion motion. For higher generations, back-folding should be more extensive, leading to lower libration amplitudes. In these materials, thermal energy is dissipated preferentially through mobility at the secondary amide sites. The dendrimer structures are stabilized by hydrogen bonding between protonated tertiary amines and chloride anions at the branching points and, to some extent, between amide and carboxylic oxygen atoms of neighboring branches. The average hydrogen bond distance was approximately the same for both types of bonding, and its distribution is narrow, indicating highly uniform environments. The breaking of stabilizing hydrogen bonds results in growing amplitudes of motion inside the polymer network, up to the point where material starts to flow. Around generation 3, steric crowding at the dendrimer surface hinders deep interpenetration between neighboring molecules. The structural change to a folded architecture may occur over several generations (3−5)[15] and is probably a generic property of dendritic polymers.

PAMAM behavior is determined by the interplay between stabilizing effects of hydrogen bonding and destabilizing effects of molecular motion. Temperature-dependent line shapes of ND_3^+ groups are explained by large angle, asymmetric libration of terminal groups, perhaps located in the voids of the dendrimer network. Unequal site populations, due to a preference for sites with stronger bonding to Cl^-, are required to account for the observed asymmetry of the ND_3^+ powder patterns.

To help increase spectral resolution, determine intra- and intermolecular distances, and obtain more precise quantitative information on the rates and activation energies of molecular motion, different solid NMR techniques (e.g., REDOR,[47] dueteron MAS,[48] as well as T_{1Z} and T_{1Q} relaxation studies) should be applied. Our findings about PAMAM T_{1Z} relaxation will be discussed in a future publication. For dendrimers with flexible spacers, like PAMAM, the effect of molecular motion is strongly pronounced and has to be carefully considered before planning and interpreting REDOR experiments.[47]

To obtain a complete quantitative picture of dendrimer structure and motion, it will be essential to apply a combination of experimental NMR techniques as well as more traditional methods of polymer characterization.

Acknowledgment. This work was supported in part by National Science Foundation Grants CHE 9701014 and DMR 9973933. The authors are grateful to the Michigan Molecular Institute Dendritech Inc. (http://www.mmi.org/mmi/dendritech/pamam.html) for supplying high numbered generations of material for the present study.

References and Notes

(1) Hawker, C. J.; Frechet, J. M. J. In *New Methods of Polymer Synthesis*; Ebdon, J. R., et al., Eds.; UK: Blackie, Glasgow, 1995; pp 290−330.
(2) Newkome, G. R.; Moorefield, C. N.; Voegtle, F. *Dendritic Molecules. Concepts−Synthesis−Perspectives*; VCH Publishers: New York, 1996; Chapter 10.
(3) Tomalia, D. A.; Baker, H.; Dewald, J.; Hall, M.; Kallos, G.; Martin, S.; Roeck, J.; Ryder, J.; Smith, P. *Macromolecules* **1986**, *19*, 2486.
(4) Uppuluri, S.; Tomalia, D. A.; Dvornic, P. R. In *Polymeric Materials Encyclopedia*; Salamone, J. C., Ed.; CRC Press: New York, 1996; Vol. 3, pp 1824−1830.
(5) Tomalia, D. A.; Durst, H. D. In *Topics in Current Chemistry*; Weber, E., Ed.; Springer-Verlag: Berlin, 1993; Vol. 165, pp 193−313.
(6) Uppuluri, S.; Tomalia, D. A.; Dvornic, P. R. *Polym. Mater. Sci. Eng.* **1997**, *77*, 116−117.
(7) Karplus, M. *Physica* **1999**, *263*, 389−391.
(8) Matthews, B. R.; Holan, G. *Antiviral Polyamidoamine Dendrimers*. AU Appl 94/6,239, June 1994; 47 pp.
(9) Poxon, S. W.; Mitchell, P. M.; Liang, E.; Hughes, J. A. *Drug Delivery* **1996**, *3*, 255−261.
(10) Sayed-Sweet, Y.; Hedstrand, D. M.; Spinder, R.; Tomalia, D. A. *J. Mater. Chem.* **1997**, *7*, 1199−1205.
(11) Wiener, E. C.; Brechbiel, M. W.; Brothers, H.; Magin, R. L.; Gansow, O. A.; Tomalia, D. A.; Lauterbur, P. C. *Magn. Res. Med.* **1994**, *31*, 1−8.
(12) Tsukruk, V. V.; Rinderspacher, F.; Bliznyuk, V. N. *Langmuir* **1997**, *13*, 2171−2176.
(13) Meltzer, A. D.; Tirrell, D. A.; Jones, A. A.; Inglefield, P. T. *Macromolecules* **1992**, *25*, 4549−4552.
(14) Meltzer, A. D.; Tirrell, D. A.; Jones, A. A.; Inglefield, P. T.; Hedstrand, D. M.; Tomalia, D. A. *Macromolecules* **1992**, *25*, 4541−4548.
(15) Naylor, A. M.; Goddard, W. A. I. *J. Am. Chem. Soc.* **1989**, *111*, 2339−2341.
(16) Amis, E. J.; Topp, A.; Bauer, B. J.; Tomalia, D. A. *Polym. Mater. Sci. Eng.* **1997**, *77*, 183−184.
(17) Prosa, T. J.; Bauer, B. J.; Amis, E. J.; Tomalia, D. A.; Scherrenberg, R. *J. Polym. Sci., Part B: Polym. Phys.* **1997**, *35*, 2913−2924.
(18) Lescanec, R. L.; Muthukumar, M. *Macromolecules* **1990**, *23*, 2280−2288.
(19) De Gennes, P. G.; Hervet, H. *J. Phys., Lett.* **1983**, *44*, 351−360.
(20) Moreno-Bondi, M. C.; Orellana, G.; Turro, N. J.; Tomalia, D. A. *Macromolecules* **1990**, *23*, 910−912.
(21) Ottaviani, F. M.; Bossmann, S.; Turro, N. J.; Tomalia, D. A. *J. Am. Chem. Soc.* **1994**, *116*, 661−671.
(22) Ottaviani, F. M.; Montani, F.; Turro, N. J.; Tomalia, D. A. *J. Phys. Chem. B* **1997**, *101*, 158−166.
(23) Gopidas, K. R.; Leheny, A. R.; Caminati, G.; Turro, N. J.; Tomalia, D. A. *J. Am. Chem. Soc.* **1991**, *113*, 7335−7342.
(24) Gao, Y.; Langley, K. I.; Karasz, F. E. *Macromolecules* **1992**, *25*, 4902−4904.
(25) Valachovic, D. E. *Polym. Mater. Sci. Eng.* **1997**, *77*, 230−231.
(26) van Genderen, M. H. P.; Baars, M. W. P. L.; Elissan-Roman, C.; de Brabender-vanden Berg, E. M. M.; Meijer, E. W. *Polym. Mater. Sci. Eng.* **1995**, *73*, 336−337.
(27) Gruwel, M. L. H.; Wasylishen, R. E. *Z. Naturforsch.* **1991**, *46A*, 691−696.
(28) Gruwel, M. L. H.; Wasylishen, R. E. *Z. Naturforsch.* **1992**, *47A*, 1073−1086.
(29) Gerald, R.; Bernhard, T.; Haeberlen, U.; Rendell, J.; Opella, S. *J. Am. Chem. Soc.* **1993**, *115*, 777−782.
(30) Usha, M. G.; Peticolas, W. L.; Wittebort, R. J. *Biochemistry* **1991**, *30*, 3955−3962.
(31) Hunt, M. J.; Mackay, A. L. *J. Magn. Reson.* **1976**, *22*, 295−301.
(32) Hunt, M. J.; Mackay, A. L. *J. Magn. Reson.* **1973**, *15*, 402−414.
(33) Varner, S. J.; Vold, R. L.; Hoatson, G. L. *J. Magn. Reson. A* **1996**, *123*, 72−80.
(34) Bloom, M.; Davis, J. H.; Valic, M. I. *Can. J. Chem.* **1980**, *58*, 1510−1520.
(35) Schuster, P.; Zundel, G.; Sandorfy, C. *The Hydrogen Bond*; North-Holland Publishing Company: New York, 1976; Vol. 2, p 910.
(36) Vaughan, P.; Donohue, J. *Acta Crystallogr.* **1952**, *5*, 530−535.
(37) Chiba, T. *Bull. Chem. Soc. Jpn.* **1965**, *38*, 259.
(38) Heaton, N. J.; Vold, R. L.; Vold, R. R. *J. Am. Chem. Soc.* **1989**, *111*, 3211−3217.
(39) Harris, K. D. M.; Thomas, J. M. *J. Chem. Soc., Faraday Trans.* **1990**, *86*, 2985.
(40) LiWang *J. Magn. Reson.* **1997**, *127*, 54−64.
(41) Brink, D. M.; Satchler, G. R. *Angular Momentum*; Oxford University Press: Oxford, 1968.
(42) Wittebort, R. J.; Olejniczak, E. T.; Griffin, R. G. *J. Chem. Phys.* **1987**, *86*, 5411−5420.
(43) *Handbook of Chemistry and Physics*; Lide, D. R., Ed.; CRC Press: New York, 1996−1997; pp 9−34.
(44) Bosman, A. W.; Bruining, M. J.; Kooijman, H.; Spek, A. L.; Janssen, R. A. J.; Meijer, E. W. *J. Am. Chem. Soc.* **1998**, *120*, 8547−8548.
(45) Uppuluri, S. Ph.D. Dissertation Thesis, Michigan Technoligical University, Houghton, MI, 1997.
(46) Wooley, K. L.; Klug, C. A.; Tasaki, K.; Schaefer, J. *J. Am. Chem. Soc.* **1997**, *119*, 53−58.
(47) Goetz, J. M.; Schaefer, J. *J. Magn. Reson.* **1997**, *127*, 147−154.
(48) Maricq, M. M.; Waugh, J. S. *J. Chem. Phys.* **1979**, *70*, 3300−3316.

MA9916178